

Near-field imaging by a micro-particle: a model for conversion of evanescent photons into propagating photons

Djenan Ganic, Xiaosong Gan, and Min Gu

Centre for Micro-Photonics, School of Biophysical Sciences and Electrical Engineering
Swinburne University of Technology, P.O. Box 218, Hawthorn 3122, Australia
mgu@swin.edu.au

Abstract: In this letter we present a physical model, both theoretically and experimentally, which describes the mechanism for the conversion of evanescent photons into propagating photons detectable by an imaging system. The conversion mechanism consists of two physical processes, near-field Mie scattering enhanced by morphology dependant resonance and vectorial diffraction. For dielectric probe particles, these two processes lead to the formation of an interference-like pattern in the far-field of a collecting objective. The detailed knowledge of the far-field structure of converted evanescent photons is extremely important for designing novel detection systems. This model should find broad applications in near-field imaging, optical nanometry and near-field metrology.

© 2004 Optical Society of America

OCIS codes: (260.1960) Diffraction theory; (110.2990) Image formation theory; (140.7010) Trapping

References and links

1. E. Betzig and J. K. Trautman, "Near-field optics: Microscopy, spectroscopy, and surface modification beyond the diffraction limit," *Science* **257**, 189-195 (1992).
2. J. Koglin, U. C. Fischer, and H. Fuchs, "Material Contrast in Scanning Near-Field Optical Microscopy (SNOM) at 1-10 nm Resolution," *Phys. Rev. B* **55**, 7977-7984 (1997).
3. F. Zenhausern, Y. Martin, and H. K. Wickramasinghe, "Scanning Interferometric Apertureless Microscopy: Optical Imaging at 10 Angstrom Resolution," *Science* **269**, 1083-1085 (1995).
4. U. C. Fischer and D. W. Pohl, "Observation of single-particle plasmons by near-field optical microscopy," *Phys. Rev. Lett.* **62**, 458-461 (1989).
5. R. X. Bian, R. C. Dunn, X. S. Xie, and P. T. Leung, "Single molecule emission characteristics in near-field microscopy," *Phys. Rev. Lett.* **75**, 4772-4775 (1995).
6. W. P. Ambrose, P. M. Goodwin, J. C. Martin, and R. A. Keller, "Single molecule detection and photochemistry on a surface using near-field optical excitation," *Phys. Rev. Lett.* **72**, 160-163 (1994).
7. J. C. Weeber, E. Bourillot, A. Dereux, J. P. Goudonnet, Y. Chen, and C. Girard, "Observation of light effects with a near-field optical microscope," *Phys. Rev. Lett.* **77**, 5332-5335 (1996).
8. L. Novotny, R. X. Bian, and X. S. Xie, "Theory of nanometric optical tweezers," *Phys. Rev. Lett.* **79**, 645-648 (1997).
9. K. Okamoto and S. Kawata, "Radiation force exerted on subwavelength particles near a nanoaperture," *Phys. Rev. Lett.* **83**, 4534-4537 (1999).
10. E. H. Syngé, "A suggested method for extending the microscopic resolution into the ultramicroscopic region," *Phil. Mag.* **6**, 356-362 (1928).
11. D. McMullan, "The prehistory of scanned image microscopy Part 1: scanned optical microscopes," *Proc. R. Microsc. Soc.* **25**, 127-131 (1990).
12. R. C. Reddick, R. J. Warmack, and T. L. Ferrell, "New form of scanning optical microscopy," *Phys. Rev. B* **39**, 767-770 (1989).
13. T. Sugiura, T. Okada, Y. Inouye, O. Nakamura, and S. Kawata, "Gold-bead scanning near-field optical microscope with laser-force position control," *Opt. Lett.* **22**, 1663-1665 (1997).
14. U. Dürrig, D. W. Pohl, and F. Rohner, "Near-field optical-scanning microscopy," *J. Appl. Phys.* **59**, 3318-3327 (1986).
15. R. Carminati and J. J. Sáenz, "Scattering theory of Bardeen's formalism for tunneling: New approach to near-field microscopy," *Phys. Rev. Lett.* **84**, 5156-5159 (2000).

16. M. Gu and P. C. Ke, "Image enhancement in near-field scanning optical microscopy with laser-trapped metallic particles," *Opt. Lett.* **24**, 74-76 (1999).
 17. M. Gu and P. C. Ke, "Effect of depolarization of scattering evanescent waves on near-field imaging with laser-trapped particles," *Appl. Phys. Lett.* **75**, 175-177 (1999).
 18. Y. Inouye and S. Kawata, "Near-field scanning optical microscope with metallic probe tip," *Opt. Lett.* **19**, 159-161 (1994).
 19. Y. Ishii and T. Yanagida, "Single molecule detection in life science," *Single Mol.* **1**, 5-16 (2000).
 20. W. C. Liu and M. W. Kowarz, "Vector diffraction from subwavelength optical disk structures: Two-dimensional near-field profiles," *Opt. Express* **2**, 191-197 (1998).
 21. D. Ganic, X. Gan, and M. Gu, "Parametric study of three-dimensional near-field Mie scattering by dielectric particles," *Opt. Commun.* **216**, 1-10 (2003).
 22. H. Chew, D. Wang, and M. Kerker, "Elastic scattering of evanescent electromagnetic waves," *Appl. Opt.* **18**, 2679-2687 (1979).
 23. J. Enderlein, "Theoretical study of detection of a dipole emitter through an objective with high numerical aperture," *Opt. Lett.* **25**, 634-636 (2000).
 24. B. Ovryn and S. H. Izen, "Imaging of transparent spheres through a planar interface using a high-numerical-aperture optical microscope," *J. Opt. Soc. Am. A* **17**, 1202-1213 (2000).
 25. B. Richards and E. Wolf, "Electromagnetic diffraction in optical systems, II. Structure of the image in an aplanatic system," *Proc. Royal. Soc. A.* **253**, 358-379 (1959).
 26. M. Born and E. Wolf, *Principles of optics*, (Cambridge University Press, Cambridge 1999).
-

1. Introduction

Optical near-field imaging has become a rich research field in recent years due to its ability to achieve optical resolution well below the classical diffraction limit of approximately half the wavelength of illuminating light. The principle of this imaging technique is to probe the near field of an object under investigation, and thereby extract high-resolution information about the object which otherwise does not reach a far-field detector. The most widely applied near-field imaging technique is scanning near-field optical microscopy (SNOM) [1]. Applying SNOM techniques one has achieved optical superresolution in the range of 1-10 nm [2,3]. The SNOM technique is utilized in various high-resolution applications such as single-particle plasmons observations [4], single molecule detection experiments [5,6], light confinement studies [7] and trapping and manipulation of nano-scale objects [8,9].

Near-field imaging (NFI), implemented using SNOM techniques, can generally be classified into three categories: scanning aperture type [10,11], frustrated total internal reflection (FTIR) illumination with fibre tip collection [12] and total internal reflection illumination (TIR) with scattering collection [13]. The scanning aperture type NFI utilizes a subwavelength-diameter aperture as a localized evanescent field source. The aperture is scanned along a sample in a close proximity, typically a few nanometers, and the transmitted signal is collected by a conventional optical system. The theoretical treatment of image formation of this type of NFI has been well dealt with [14]. NFI implemented with FTIR illumination and fibre tip collection probes a sample modulated by a localized evanescent field and collects evanescent photons through the photon tunnelling process. The physical model for describing the signal collection with this type of NFI is analogous to the electron tunnelling process in scanning tunnelling microscopy [15]. The third NFI category employs TIR illumination to generate evanescent field. The field is probed using a small scatterer, such as a microscopic metallic or dielectric particle or a metallic needle, to convert evanescent photons into propagating photons [16,17]. While the conversion mechanism by a metallic needle has been studied [18], to our knowledge, the underlying physical principle of the mechanism for the evanescent photon conversion by a microscopic particle probe, such as the one utilized with the trapped particle SNOM [16,17], has not been dealt with. Such a physical understanding is also needed in nanometry for single molecule detection, in which case a single molecule is attached to a laser trapped microscopic particle immersed into evanescent field, and is monitored by measuring the scattered field [19]. The aim of our paper is to study the process of the evanescent photon conversion by a microscopic particle situated at an interface at which an evanescent wave is generated. The model can also be applied to consider

the trapped particle SNOM [16,17] and optical trap nanometry for single molecule detection [19].

This article is structured as follows. In Section 2 we describe our physical model and underlying mathematical treatment of the problem. In Section 3 we present model predictions for dielectric particles of various sizes. Experimental results and model predictions comparison is also given. Pinhole detection of the collected signal, scattered by a small dielectric particle, is investigated in Section 4. Finally, conclusions are drawn in Section 5.

2. Physical model

Our physical model of the evanescent photon conversion mechanism is based on near-field Mie scattering enhanced by morphology dependent resonance (MDR) and vectorial diffraction by a high numerical aperture (NA) lens. The importance of the vectorial diffraction approach for the treatment of the scattered field was already pointed out by Liu and Kowarz [20]. To discuss the mathematical treatment of this problem, we first present our analytical expression for the three-dimensional vectorial field distribution around a microscopic particle immersed in an evanescent field. It is derived in the framework of near-field Mie scattering when a particle is situated in a close proximity of the surface on which an evanescent field is generated [21]. The influence of the surface is also taken into account. Subsequently, we include the effect of the trapping/collecting objective by investigating the vectorial diffraction process, to determine the focal intensity distribution (FID) in the image space focal region of the collecting high NA objective. The trapping/collecting objective is one objective which is used for both trapping of a microscopic particle and for collecting the scattered signal. From now on we refer to this objective as the collecting objective only.

Let us consider a microscopic particle in a close proximity of the interface at which an evanescent field is generated by the TIR ($\alpha > \alpha_c$) under either transverse electric (TE) or transverse magnetic (TM) incident illumination (Fig. 1(a)). The origin of our coordinate system is located at the center of the particle with a coordinate systems defined in Fig. 1(a). The particle is observed by a high NA objective whose focal point coincides with the particle center. The evanescent wave generated by TIR propagates in the Y_1 direction and decays exponentially in the Z_1 direction, while interacting with the microscopic particle. This interaction can be physically described in terms of superposition of the field scattered by the microscopic particle into upper space (space above the prism surface) and partial reflection of the scattered field into the bottom space (space below the prism surface). The scattered field for TE illumination is given by Eq. (1), while the full treatment of this physical process is given elsewhere [21].

$$\begin{aligned} \mathbf{E}_{sc}(\mathbf{r}) = \sum_{lm} \left\{ \frac{c\beta_E(l,m)}{n'^2\omega\sqrt{l(l+1)}} \frac{h_l^{(1)}(k'r)}{r\sin\theta} \left[\frac{\partial}{\partial\theta} \left(\frac{\partial Y_{lm}}{\partial\theta} \sin\theta \right) + \frac{1}{\sin\theta} \frac{\partial^2 Y_{lm}}{\partial\varphi^2} \right] \mathbf{r}_1 \right. \\ \left. + \left[\frac{(-1)\beta_M(l,m)h_l^{(1)}(k'r)}{i\sin\theta\sqrt{l(l+1)}} \frac{\partial Y_{lm}}{\partial\varphi} - \frac{c\beta_E(l,m)}{n'^2\omega\sqrt{l(l+1)}} \frac{1}{r} \frac{\partial Y_{lm}}{\partial\theta} \frac{\partial}{\partial r} (rh_l^{(1)}(k'r)) \right] \boldsymbol{\theta}_1 \right. \\ \left. + \left[\frac{\beta_M(l,m)h_l^{(1)}(k'r)}{i\sqrt{l(l+1)}} \frac{\partial Y_{lm}}{\partial\theta} - \frac{c\beta_E(l,m)}{n'^2\omega\sqrt{l(l+1)}} \frac{1}{r\sin\theta} \frac{\partial Y_{lm}}{\partial\varphi} \frac{\partial}{\partial r} (rh_l^{(1)}(k'r)) \right] \boldsymbol{\varphi}_1 \right\}. \quad (1) \end{aligned}$$

In Eq. (1), \mathbf{r}_1 , $\boldsymbol{\theta}_1$ and $\boldsymbol{\varphi}_1$ are the unit vectors in the spherical coordinate system, $l = 1$ to ∞ and $m = -l$ to $+l$. k' is the wave number and n' is the refractive index of the medium in which a particle probe is immersed. c is the speed of light in vacuum and ω is the angular frequency of the incident light. The functions $\beta_E(l,m)$ and $\beta_M(l,m)$ are the expansion coefficients relating the

illumination evanescent field, $h_l^{(1)}(k'r)$ is the spherical Hankel function of the first kind. θ and φ are the variables of the scalar spherical harmonics Y_{lm} . In the case of TM illumination the scattered field is also given by Eq. (1) with expansion coefficients $\beta_E(l, m)$ and $\beta_M(l, m)$ substituted by $\tilde{\beta}_E(l, m)$ and $\tilde{\beta}_M(l, m)$, respectively [22].

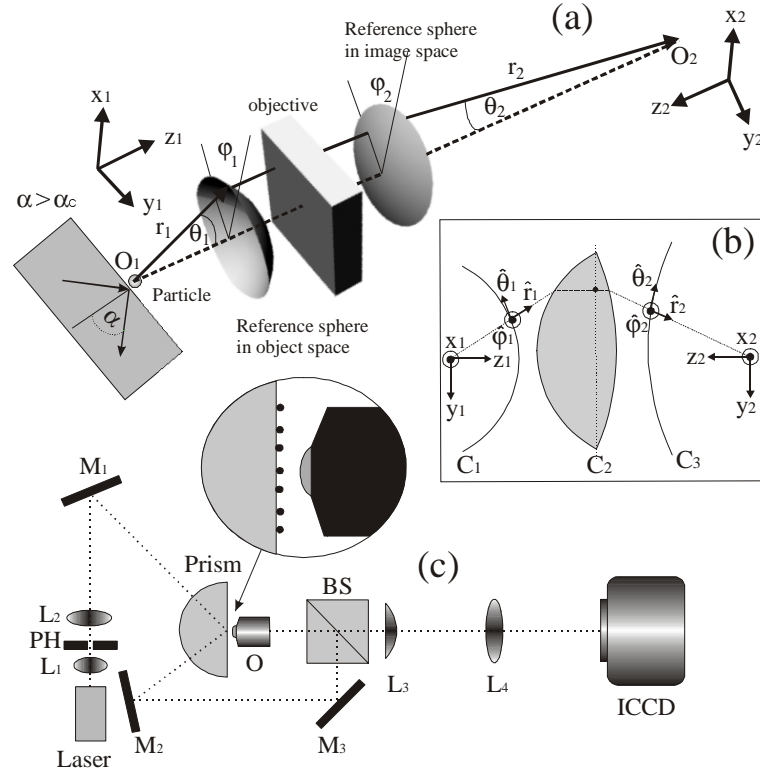


Fig. 1. (a) Schematic of our theoretical model for evanescent photon conversion. (b) Representation of the lens transformation process. (c) Experimental setup for recording the FID of converted evanescent photons, collected by a high NA objective.

Using this method one can calculate the superposed scattered field on the reference sphere in object space. The center of this reference sphere (also known as the entrance pupil of the collecting objective) overlaps with the particle center, i.e., the origin of our coordinate system O_1 . The shadowing effects are neglected in this process. The reason that the shadowing effects could be neglected is because they occur for the reflected portion of the scattered field from the prism surface incident at low angles with respect to the surface normal. At such angles the Fresnel reflection coefficients indicate that only ~4% of incident light is reflected. Furthermore, the field scattered by dielectric particles is the most strongly scattered in the direction at high angles with respect to the surface normal (forward direction) [21]. These two effects indicate that the reflected field contributing to the shadowing effects is 2-3 orders of magnitude weaker than the contribution of the field reflected at high angles, and therefore could be neglected.

The precise transformation of the field from the reference sphere in object space to the field on the reference sphere in image space requires a detailed model of the lens. Recent studies of imaging dipole emitters [23] and microscopic particles [24] through a high NA objective have indicated that we can assume that the imaging objective transforms a diverging spherical wave with its origin O_1 in the center of the particle into a converging spherical wave

whose origin O_2 is in the center of the focal region in image space. Therefore, the lens effect can physically be modeled as a retardation effect affecting the wave traversing two different dielectric media (air and glass). Consider the spherical wavefront C_1 originating from the particle center O_1 (the origin of the coordinate system $X_1Y_1Z_1$), just before the collecting lens (Fig. 1(b)). Its curvature corresponds exactly to the curvature of the collecting lens in object space. After traversing the lens front surface, the wavefront becomes the plane wavefront C_2 . All points on the spherical wavefront C_1 arrive at the plane wavefront C_2 at the same time. The plane wavefront is then similarly transformed to the converging spherical wavefront C_3 , after traversing the lens back surface. The center of the spherical wavefront C_3 is at O_2 (the origin of the coordinate system $X_2Y_2Z_2$). Such transformation further indicates that the lens imparts a scaling effect and a vector rotation. If we consider scattered field vector components, described by its unit vectors $\hat{\mathbf{r}}_1$, $\hat{\boldsymbol{\theta}}_1$, and $\hat{\boldsymbol{\phi}}_1$ in coordinate system $X_1Y_1Z_1$, they are transformed into $-\hat{\mathbf{r}}_2$, $\hat{\boldsymbol{\theta}}_2$, and $\hat{\boldsymbol{\phi}}_2$ in coordinate system $X_2Y_2Z_2$.

Considering such a transformation process of the field from the entrance pupil to the exit pupil, the focal field distribution in image space can be derived by the vectorial diffraction process as given by Richards and Wolf [25],

$$\mathbf{E}(r_2, \psi, z_2) = \frac{i}{\lambda} \iint_{\Omega} \left(-E_{r_1} \hat{\mathbf{r}}_2 + E_{\theta_1} \hat{\boldsymbol{\theta}}_2 + E_{\phi_1} \hat{\boldsymbol{\phi}}_2 \right) \exp[-ikr_2 \sin \theta_2 \cos(\varphi_2 - \psi)] \times \exp(-ikz_2 \cos \theta_2) \sin \theta_2 d\theta_2 d\varphi_2, \quad (2)$$

where E_{r_1} , E_{θ_1} and E_{ϕ_1} are given by Eq. (1), while r_2 , ψ and z_2 are cylindrical coordinates of a point in image space with a coordinate system shown in Fig. 1(a).

3. Theoretical and experimental results

Applied to evanescent photon conversion by a small dielectric particle probe for either TE or TM incident illumination, our model leads to the FID in the far-field of the collecting lens, similar to the one obtained for imaging a dipole emitter (Fig. 2(a) and 2(e)).

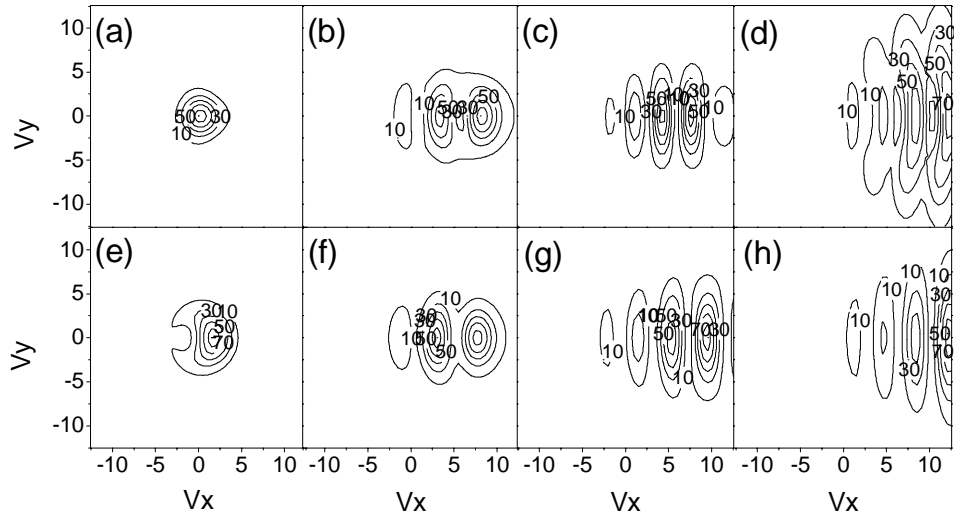


Fig. 2. Calculated FID in the image focal plane of a 0.8 NA objective. TE (top row) and TM (bottom row) incident illumination. (a) and (e) $a=100$ nm. (b) and (f) $a=500$ nm. (c) and (g) $a=1000$ nm. (d) and (h) $a=2000$ nm. Particle refractive index is 1.59, and illumination wavelength is 633 nm. All figures are normalised to 100.

This is not surprising, as the probe in this case is much smaller than the wavelength of illuminating light, and the particle is completely immersed into the evanescent field, so the dipole approximation applies. However, when the particle radius approaches and exceeds the wavelength of the illuminating light, the FID shows a complex interference-like structure (Figs. 2(b)-2(d) and 2(f)-2(h)). Furthermore, our model indicates that the conversion and collection of TE evanescent photons is somewhat different from TM evanescent photons (Fig. 2). The FID in image space of the collecting lens shows a similar interference-like structure for the conversion of either TE or TM localized photons by large particles. However, when the conversion is performed by a small particle, this similarity in the FID is less pronounced.

The complex interference-like pattern shown in Fig. 2 arises due to the enhancement of MDR and higher multipoles, scattering properties of large particles and the effects of the interface on which the evanescent field is generated. MDR is a well-known physical effect, which results in an increase in the scattered intensity caused by the constructive interference of electromagnetic waves traveling inside a narrow domain in vicinity of the particle surface, i.e. confined by an almost TIR. One would expect to see the MDR effects in the FID of the collecting objective, due to the increase in the collected energy. These effects are indeed manifested in the FID of our model. Two particular MDR for TE and TM polarized incident illumination are shown in Fig. 3, however the same argument is equally valid for other MDR positions [21]. The FID images indicate that the effect of MDR is not just a mere increase in collected energy due to a particular MDR, but also leads to different energy distribution for on and off resonance positions (Fig. 3 insets). The increase in the maximal collected intensity at the two MDR positions is approximately 50 times. This different energy distribution outlines the importance of detector selection for systems operating at MDR positions, because it would be an advantage to operate particle trapped SNOM and optical trap nanometry systems at MDR positions to enhance signal-to-noise ratio. In the case of a pinhole detector a particular attention needs to be paid to the pinhole size, which needs to be appropriately selected to collect all of the available signal.

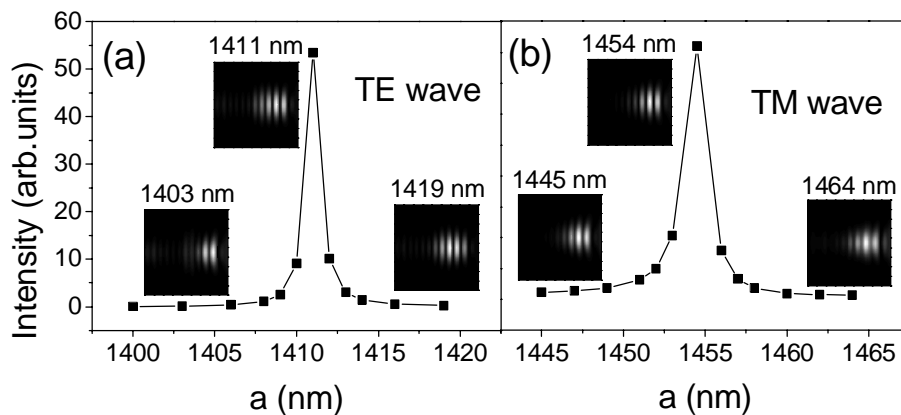


Fig. 3. Maximum intensity in the FID as a function of the particle radius near MDR for TE (a) and TM (b) illumination. Insets show the full normalized FID representing off and on resonance cases. Insets FID images are centered in the focal plane and their size is $220 \mu\text{m} \times 220 \mu\text{m}$. Particle refractive index is 1.59, and illumination wavelength is 633 nm.

To confirm the conversion mechanism given by our model we have conducted an experiment. The experimental setup is depicted in Fig. 1(c). A helium-neon laser beam was expanded and filtered using lenses L_1 , L_2 and a pinhole (PH). It was then directed onto the

prism-air surface by mirror M_1 to form an incident angle of 51° , which was well above the critical angle (α_c). The prism used in the experiment had a refractive index of 1.722 and the particles under investigation were polystyrene particles diluted in water and dried on the prism surface. The particles, immersed into the created localized field, were imaged using a dry 0.8 NA objective (Olympus IC 100, infinite tube length) and projected onto an intensified CCD camera (PicoStar HR 12 from LaVision) via lenses L_3 and L_4 . The TIR portion of the incident beam was re-routed via mirrors M_2 and M_3 and a beam-splitter (BS) into the back aperture of the collecting objective (O), to enable us to locate the prism surface and thus the center of the particle under consideration. The calculated and observed results of the FID of the collecting objective, for the conversion of both TE and TM evanescent photons by a polystyrene particle of 240 nm in radius, are shown in Fig. 4.

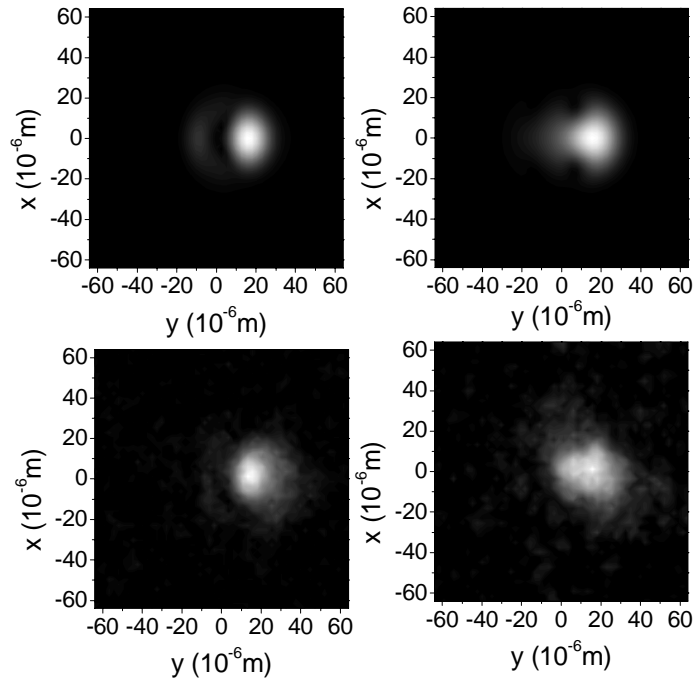


Fig. 4. Calculated (top) and observed (bottom) FID in image focal plane of a 0.8 NA objective collecting propagating photons converted by $a=240$ nm polystyrene particle under TE (left column) and TM (right column) incident illumination.

It can be seen from Fig. 4 that the FID structure predicted by our model is in good agreement with the experimentally observed results. Furthermore, the predicted difference in the FID structure for TE and TM evanescent photons converted by this small dielectric probe is observable in the experiment.

The interference-like FID structure for evanescent photon conversion by a large dielectric particle probe can also be experimentally observed. Figure 5(a) shows our calculated result of the FID for evanescent photon conversion by a $1 \mu\text{m}$ (radius) polystyrene particle. The corresponding experimentally observed result is shown in Fig. 5(b). Image resolution of the observed result is somewhat degraded due to the imaging properties of lens L_4 . The observed structure is a result of the convolution of the point-spread function (PSF) of the imaging lens L_4 and the calculated result shown in Fig. 5(a). The agreement between calculated and experimental results confirm that the conversion of evanescent photons is the result of two physical processes, near-field Mie scattering and vectorial diffraction.

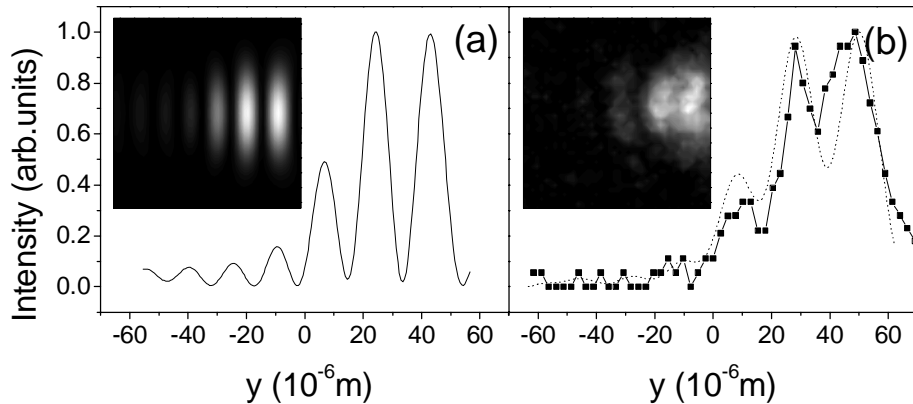


Fig. 5. Calculated and observed y axis scan through $x=0$, in image focal plane of a 0.8 NA objective collecting propagating photons converted by 1000 nm (radius) polystyrene particle under TE incident illumination. (a) Calculated results. (b) Observed results (full line) where the dotted line represents the convolution of the calculated results and the PSF of the imaging lens. Insets show the calculated and observed FID.

4. Signal level

In this section we will look at the signal level of the scattered near-field signal, determined using our physical model described in the previous section, by a pinhole detector. Such a detector is utilized in the trapped particle SNOM to discriminate against the out of focus signal. Pinhole detector is essentially a small circular opening of a few to several tens of micrometers, in an otherwise opaque screen, placed perpendicularly to the optical axis at the back focal plane of the imaging objective. The back focal plane focus coincides with the center of the pinhole. Only the signal that can pass through this opening is detected, and it constitutes of the signal coming from the front focal region of the imaging objective (Fig. 6 (a)).

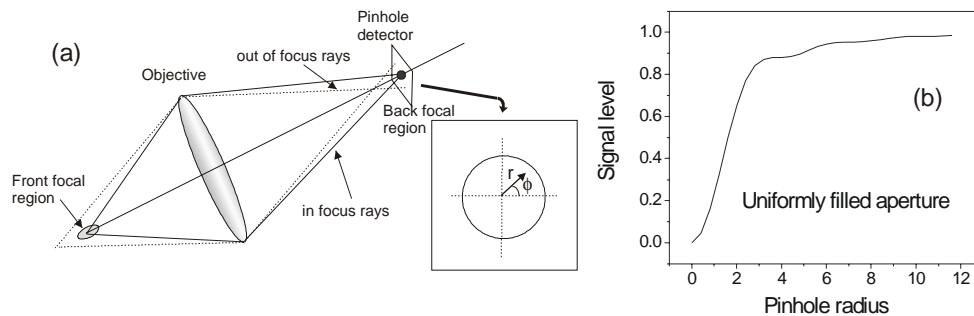


Fig. 6. (a) A schematic diagram of a pinhole detection process. Only the rays coming from the front focal region are detected. (b) Detected signal intensity as a function of a pinhole radius, in optical coordinates, for uniformly illuminated objective. Assumed objective NA = 0.8 in the front focal region, aperture size $\rho_a = 3$ mm and the back focal length of the objective $f = 160$ mm.

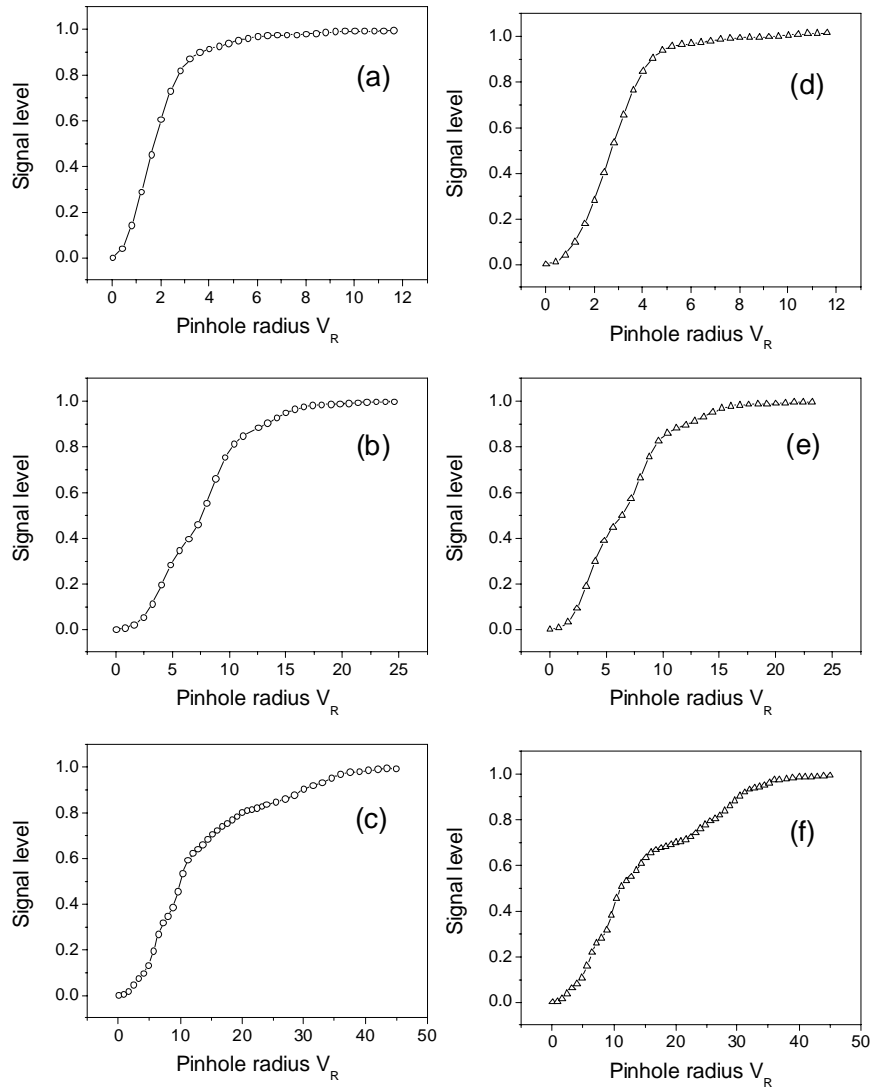


Fig. 7. Scattered level as a function of pinhole size (in optical coordinates) of a polystyrene particle for TE illumination (left column) and TM illumination (right column). Assumed objective $\text{NA} = 0.8$ in the front focal region, aperture size $\rho_a = 3$ mm and the back focal length of the objective $f = 160$ mm. (a) and (d) Particle radius $0.1 \mu\text{m}$. (b) and (e) Particle radius $0.5 \mu\text{m}$. (c) and (f) Particle radius $1.0 \mu\text{m}$. Signal level is defined as the signal intensity normalized by the total signal intensity when pinhole radius $R \rightarrow \infty$.

Mathematically, the signal level η of a pinhole detector can be expressed as

$$\eta = \frac{\int_0^R \int_0^{2\pi} I(r, \phi) r dr d\phi}{\int_0^\infty \int_0^{2\pi} I(r, \phi) r dr d\phi}, \quad (3)$$

where R denotes the pinhole radius and $I(r, \phi)$ is the intensity at a point within the pinhole detector determined by distance r from the center of the pinhole and an angle ϕ . If we express the pinhole radius R in optical coordinates V_R defined as $V_R = 2\pi\rho_a R / (\lambda f)$, where ρ_a denotes objective aperture radius and f is the back focal length of the objective, then the signal level as function of the pinhole size for a uniformly filled aperture is shown in Fig. 6(b). This result is essentially the same as that given by Born and Wolf [26] for the fraction of the total energy contained within circles of prescribed radii (varying pinhole size), in the Fraunhofer diffraction pattern of a circular aperture.

Equation (3) can be used with the intensity $I(r, \phi)$ determined by our scattering model (Eq. (2)) for any point within the pinhole detector. Performing the appropriate integration in Eq. (3) determined by the pinhole size, the signal level can be evaluated for the two polarization states of the incident illumination and a range of pinhole sizes and scattering particles. If we consider a polystyrene scattering particle, the signal level of a pinhole detector is shown in Fig. 7. It can be seen that for very small particles (Figs. 7(a) and (d)) the signal is similar to the signal for a uniformly filled aperture (Fig. 6(b)). This is because a very small particle behaves as a point source and at a far-field distance the scattered signal fills the entrance pupil of the objective nearly uniformly. For the wavelength-size particles (Figs. 7(b) and (e)) much larger pinhole size is required to collect the signal completely. For the typical conditions given in Fig. 7, it can be estimated that a pinhole of a radius of 80 μm is required to collect the total signal for either TE or TM incident illumination. The scattering properties of large particles, manifested mainly through the MDR and the interaction cross-section effects, result in the much larger pinhole size ($\sim 200 \mu\text{m}$) required for signal collection (Fig. 7 (c) and (f)). As we have seen in Fig. 2(d) and (h), the FID of large particles shows the spreading of the scattered signal in the forward direction, thus the requirement for a large pinhole size for total signal collection of the field scattered by large dielectric particles.

5. Conclusion

In conclusion, we have presented, both theoretically and experimentally, a physical model for the mechanism for conversion of evanescent photons into propagating photons by a small particle. This model consists of two physical processes, near-field Mie scattering enhanced by MDR and vectorial diffraction. As a result, the far-field intensity pattern of the collecting objective shows an interference-like pattern for a large dielectric particle probe, while it is similar to dipole radiation for small dielectric particles. Due to the MDR effect the energy distribution in the detection plane is different for on and off resonance conditions. This model provides an understanding of the evanescent photon conversion in trapped particle SNOM and a detailed physical picture of the energy distribution in the far-field region of a collecting objective.

When the detection of the scattered signal is performed by a pinhole detector, the detector size needs to be carefully selected depending on the scattering particle size. A very small particles act as point sources and fill the objective entrance pupil nearly uniformly. In that case, a very small pinhole ($\sim 20\text{-}30 \mu\text{m}$ in radius) is sufficient to collect the total signal. For large particles, on the other hand much larger pinholes are required to completely collect the scattered signal using a typical imaging lens. This effect is mainly caused by the MDR and larger interaction cross-section of the particle and the evanescent field, which leads to the

spreading of the scattered signal in the forward direction and thus to the spreading of the signal in the imaging plane.

Furthermore, the model also provides a tool for designing novel detection arrangements in the fields of NFI, optical trap nanometry and near-field metrology with high accuracy and resolution.

Acknowledgments

The authors thank the Australian Research Council for its support.